Fully implicit interface tracking for a viscous drop under simple shear

Fully implicit interface tracking for a viscous drop under simple shear

Christos Mitrias[a], Martien A. Hulsen[a,*], Patrick D. Anderson[a]

[a] *Department of Mechanical Engineering,*
Eindhoven University of Technology,
P.O. Box 513, 5600 MB Eindhoven, The Netherlands

Abstract

In this article we present a novel 3D implicit interface tracking method for sharp interfaces with interfacial tension in the creeping flow regime, employing the finite element method. The interface nodes are allowed to move only in the normal direction and thus remeshing can be avoided, most of the times. The implicit method allows us to overcome certain time step limitations imposed by the mesh capillary time. To validate our method, we use a fairly simple and very well understood problem of a single viscous drop suspended in a viscous matrix that deforms under an applied shear rate. This problem was first studied by Taylor [1] and has been extensively reviewed by Rallison [2] and Stone [3]. The second moment of inertia tensor was used to compute the deformation parameter D and the inclination angle θ and the results are compared to the theory for small deformations of Taylor [1].

1. Introduction

Polymer blends are widely used materials in many different applications where the final product properties depend not only on the material properties of the components, but also on the morphology of the blend [4]. Even if components forming the blend are Newtonian, the presence of elastic interfaces between the different phases results into non-Newtonian rheology of the blend. In many cases, such blends contain dispersed droplets in a continuous phase.

The deformation mechanics of a single viscous drop dispersed in a viscous matrix fluid under an imposed flow field was first studied by Taylor [1]. Taylor introduced two parameters that describe the deformation of the drop, namely the deformation parameter D and the inclination angle θ. The deformation parameter D is defined as the ratio $(a-b)/(a+b)$ where a and b are the largest and smallest distances of the drop interface from its center respectively. Hence, D is equal to zero for a sphere and becomes asymptotically unity for a slender drop. The inclination angle θ is defined as the angle between the major axis and some reference direction. The drop deformation in Newtonian fluid has be extensively reviewed by Rallison [2] and Stone [3].

*Corresponding author
Email address: M.A.Hulsen@tue.nl (Martien A. Hulsen)

There are two main classes of methods for the numerical study of problems that contain interfaces and each of them has some advantages and disadvantages. *Interface tracking methods* are focused on an accurate representation of geometric features, but in most of the cases capturing morphological changes such as coalescence and break up is extremely cumbersome [5]. On the other hand, *interface capturing methods* use an approximation by a continuous function which usually involves an additional differential equation. This way it is possible to easily model morphological changes [6]. The main drawback of interface capturing methods is the need for a choice for the width of the interface where the transition from one fluid to the other occurs. In order for simulations to remain computationally tractable, widths much larger than that of the real interface are chosen in most cases, leading to reduced accuracy [7].

Here, since we want to study only the deformation of the drop interface and not the morphological changes that can occur under certain flow conditions, we choose to use a sharp interface method employing the finite element method for discretization. This type of approach involves interface meshes that are moved over time by following the drop interface. When this is done explicitly, i.e, by separately solving the flow and interface tracking problems [8], certain time step limitations exist that depend on the size of the mesh, viscous forces and the surface tension [9, 10, 11]. To tackle this challenge, we couple the movement of the mesh nodes, both on the interface as well as in the bulk with the flow problem. The whole non-linear system consisting of the interface tracking, flow problem and update of the bulk mesh nodes, is solved using the Newton-Raphson method. A variety of fully- or semi-implicit methods using a wide range of interface tracking and interface capturing methods exist in the literature [12, 13, 14]. Nevertheless, to the best of our knowledge using interface tracking where nodes move only in the normal direction employing the finite element method as the one introduced here has never presented before.

The outline of the article is as follows. In Section 2, we first define the problem and present the mathematical model that will be used. In Section 3 the employed finite element method is presented in its linearized form. In Section 4, we proceed with the validation of the method and present the obtained results. Finally, in Section 5 we summarize with conclusions.

2. Problem definition

For the purpose of this work, the viscous drop is initially spherical with a radius R and suspended in a viscous matrix inside a cubic container of length L with $L/R = 20$. The initial geometry of the problem can be seen in Fig. 1. The dispersed drop is subjected to an imposed shear rate and starts to deform. In this section the mathematical model and its discretization using the finite element method will be described.

2.1. Governing equations

To describe the flow dynamics we assume that inertia can be neglected and that the fluid is incompressible. Therefore, the momentum and the mass balance for both the continuous and the dispersed phase reduce to

$$-\boldsymbol{\nabla} \cdot \boldsymbol{\sigma} = \mathbf{0} \quad \text{in } \Omega, \tag{1}$$

$$-\boldsymbol{\nabla} \cdot \boldsymbol{u} = 0 \quad \text{in } \Omega, \tag{2}$$

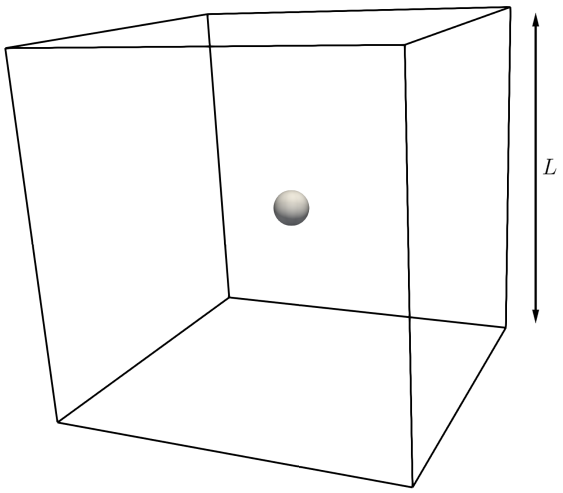

Fig. 1: Initial geometry of a single spherical drop suspended in a cubic container.

where $\boldsymbol{\sigma}$ is the stress tensor, $\boldsymbol{u}$ is the velocity vector and Ω is the area occupied by the fluids. The stress tensor $\boldsymbol{\sigma}$ is written as:

$$\boldsymbol{\sigma} = -p\boldsymbol{I} + \boldsymbol{\tau}, \tag{3}$$

where p is the pressure, $\boldsymbol{I}$ is the identity tensor and $\boldsymbol{\tau}$ is the extra stress tensor. For a Newtonian fluid the extra stress tensor is given by

$$\boldsymbol{\tau} = 2\eta\boldsymbol{D}, \tag{4}$$

where η is the viscosity with subscripts η_d for the dispersed phase and η_c for the continuous phase and $\boldsymbol{D} = (\boldsymbol{\nabla u} + (\boldsymbol{\nabla u})^T)/2$ the symmetric part of the velocity gradient tensor. Furthermore the ratio of the viscosities between the two phases is defined as $\lambda = \eta_\mathrm{d}/\eta_\mathrm{c}$.

2.2. Boundary conditions

The interface of the drops is assumed to be a material interface. Furthermore, there is no slip between the two different fluids

$$\boldsymbol{u}|_\mathrm{c} = \boldsymbol{u}|_\mathrm{d}. \tag{5}$$

The interface boundary conditions for a sharp interface lead to a jump of the stress tensor and are given by

$$\boldsymbol{\sigma}\cdot\boldsymbol{n}|_\mathrm{c} - \boldsymbol{\sigma}\cdot\boldsymbol{n}|_\mathrm{d} = \Gamma\kappa\boldsymbol{n}, \tag{6}$$

where the subscripts c and d denote the continuous and dispersed fluids respectively, Γ is the surface tension coefficient, $\boldsymbol{n}$ is the outwardly directed unit normal vector to the interface and κ is the curvature defined as

$$\kappa = \boldsymbol{\nabla}_\mathrm{s}\cdot\boldsymbol{n}, \tag{7}$$

with $\boldsymbol{\nabla}_\mathrm{s} = (\boldsymbol{I} - \boldsymbol{nn}) \cdot \boldsymbol{\nabla}$ the surface gradient operator. The domain is enclosed by solid walls where the velocity is prescribed and there is no slip between the continuous phase and the walls

$$\boldsymbol{u}|_{\partial\Omega} = \dot{\gamma} y e_x|_{\partial\Omega}, \tag{8}$$

where y is the y-coordinate of the walls $\dot{\gamma}$ the imposed shear rate and $\partial\Omega = \cup_i \partial\Omega_i$.

2.3. Interface tracking

The imposed shear rate that deforms the drop enforces an internal circulation of the fluid [15]. This motion can cause numerical difficulties by continuously deforming the mesh, and thus requiring the generation of a new mesh frequently. To avoid this issue we employ an approach similar to Villone *et al.* [8] where the interface moves with the velocity normal to it.

We describe the interface by a moving curvilinear coordinate system given by

$$\boldsymbol{x} = \bar{\boldsymbol{x}}(\underset{\sim}{\xi}, t), \tag{9}$$

where $\underset{\sim}{\xi} = (\xi^1, \xi^2)$ are the curvilinear coordinates and $\bar{\boldsymbol{x}}$ is the function that maps the coordinates $\underset{\sim}{\xi}$ onto the spatial coordinates $\boldsymbol{x}$.

The velocity of the interface for a material interface $\dot{\boldsymbol{x}}$ must be such that

$$\dot{\boldsymbol{x}} \cdot \boldsymbol{n} = \boldsymbol{u} \cdot \boldsymbol{n} \tag{10}$$

or

$$\dot{\boldsymbol{x}} = (\boldsymbol{u} \cdot \boldsymbol{n})\boldsymbol{n}, \tag{11}$$

where $\boldsymbol{u}$ is the material velocity at the interface and $\boldsymbol{n}$ is the normal vector of the surface. Note, that $\dot{\boldsymbol{x}}$ is equal to the velocity of the material in the normal direction only. In order to make the movement of the nodes on the interface Galilean frame independent the following equation for the motion of an interface has been implemented [8]

$$\dot{\boldsymbol{x}} = (\boldsymbol{u} - \boldsymbol{u}_\mathrm{c}) \cdot \boldsymbol{nn} + \boldsymbol{u}_\mathrm{c}, \tag{12}$$

where $\boldsymbol{u}_\mathrm{c}$ is the velocity of the center of volume of the bubble. Furthermore, Eq. (12) can be rewritten as

$$\dot{\boldsymbol{x}} + (\boldsymbol{u} - \boldsymbol{u}_\mathrm{c}) \cdot (\boldsymbol{I} - \boldsymbol{nn}) = \boldsymbol{u}, \tag{13}$$

where $\boldsymbol{I} - \boldsymbol{nn} = \boldsymbol{g}^\alpha \boldsymbol{g}_\alpha$ is the surface identity tensor, with $\boldsymbol{g}^\alpha$, $\alpha = 1, 2$ the dual base vectors and $\boldsymbol{g}_\alpha = \partial \boldsymbol{x} / \partial \xi^\alpha$, $\alpha = 1, 2$ are the covariant base vectors. For the term $\boldsymbol{g}^\alpha \boldsymbol{g}_\alpha$ we use the Einstein notational convention for simplifying the expression of summation. Finally, Eq. (13) can be rewritten as

$$\dot{\boldsymbol{x}} + (\boldsymbol{u} - \boldsymbol{u}_\mathrm{c}) \cdot \boldsymbol{\nabla}_\mathrm{s} \boldsymbol{x} = \boldsymbol{u}, \tag{14}$$

where $\boldsymbol{\nabla}_\mathrm{s} = \boldsymbol{g}^\alpha \dfrac{\partial}{\partial \xi^\alpha}$ is the surface gradient operator.

3. Numerical description

The mathematical model, as presented in Section 2, is solved using the finite element method. Meshes that fit the drop boundaries are employed, where the movement of the interface and bulk nodes is coupled with the flow problem. For the movement of the bulk an addition problem based on the Poisson equation is required.

3.1. Weak form

The weak form can be obtained by multiplying Eqs. (1) and (2) with test functions $\boldsymbol{v}, q$: Find $\boldsymbol{u}, p$ such that

$$(\boldsymbol{v}, -\boldsymbol{\nabla}\cdot\boldsymbol{\sigma}) = 0 \qquad \text{for all } \boldsymbol{v}, \tag{15}$$

$$(q, -\boldsymbol{\nabla}\cdot\boldsymbol{u}) = 0 \qquad \text{for all } q. \tag{16}$$

Using Eq.(3) and applying partial integration and Gauss' theorem we obtain the following weak form: Find $\boldsymbol{u}$ and p such that

$$\big((\boldsymbol{\nabla}\boldsymbol{v})^T, \boldsymbol{\tau}\big) - (\boldsymbol{\nabla}\cdot\boldsymbol{v}, p) = -\Gamma\big((\boldsymbol{\nabla}\boldsymbol{v})^T, \boldsymbol{I} - \boldsymbol{n}\boldsymbol{n}\big)_S \qquad \text{for all } \boldsymbol{v}, \tag{17}$$

$$-(q, \boldsymbol{\nabla}\cdot\boldsymbol{u}) = 0 \qquad \text{for all } q, \tag{18}$$

where (a, b) is the standard L_2 inner product in Ω and $(a, b)_S$ on surface S.

3.2. Discretization

For the discretization of the weak form we use the finite element method employing a mesh of quadratic triangles. Quadratic interpolation (P_2) for velocity and position and linear interpolation (P_1) for pressure. A second-order time discretization (BDF2) is used for the interface tracking with

$$\dot{\boldsymbol{x}} = \frac{3\boldsymbol{x}^{n+1} - 4\boldsymbol{x}^n + \boldsymbol{x}^{n-1}}{2\Delta t}, \tag{19}$$

where Δt is the time step. The mesh is discarded when the elements get too distorted and a new one is generated. That means, that in order to maintain the second order time discretization we need the positions at the previous time step $\boldsymbol{x}^{n-1}$. These are obtained by projecting the old mesh coordinates onto the new mesh [16]. If the update of the interface and bulk coordinates is done using an explicit method, the time step is limited by the mesh capillary time which is $\Delta t = \Delta x \eta_c/\Gamma$ where Δx is the minimum element size [9, 10]. To avoid time step limitations the mass and momentum balance are coupled with the update of the mesh coordinates. For that reason an additional Poisson equation is used for the movement of the mesh nodes which in its weak form using test function $\boldsymbol{w}$ reads: Find $\boldsymbol{x}$ such that

$$\big((\boldsymbol{\nabla}_n\boldsymbol{w})^T, \boldsymbol{\nabla}_n\boldsymbol{x})\big)_n = 0 \qquad \text{for all } \boldsymbol{w}, \tag{20}$$

where the subscripts $(.)_n$ indicate that for the gradient and the integration the reference coordinates at the beginning of each time step are used. The relation between $\boldsymbol{\nabla}$ and $\boldsymbol{\nabla}_n$ is given by

$$\boldsymbol{\nabla} = \boldsymbol{F}^{-T}\cdot\boldsymbol{\nabla}_n, \tag{21}$$

here $\boldsymbol{F}$ represents the deformation gradient tensor between the reference configuration Ω_n and the current configuration Ω:

$$\boldsymbol{F} = (\boldsymbol{\nabla}_n \boldsymbol{x})^T. \tag{22}$$

Eqs. (17),(18),(20), together with the interface tracking Eq. (12) as a boundary condition for the Poisson problem, are solved coupled. Noticeably, the resulting system of equations is non-linear and we want to solve it by applying the Newton-Raphson method. Hence, we have to linearize the weak form by writing

$$\boldsymbol{u} = \boldsymbol{u}_i + \delta \boldsymbol{u}, \tag{23}$$

$$p = p_i + \delta p, \tag{24}$$

$$\boldsymbol{x} = \boldsymbol{x}_i + \delta \boldsymbol{x}, \tag{25}$$

where $\boldsymbol{u}_i, p_i$ and $\boldsymbol{x}_i$ are the approximations in each iteration. This leads to a linear system of equations, where we obtain new approximations by solving for $\delta \boldsymbol{u}, \delta p$ and $\delta \boldsymbol{x}$. In order to linearize the weak form, all integrals are mapped to the fixed volume Ω_n

$$\int_{\Omega} \dots dx \rightarrow \int_{\Omega_n} \dots J \, dx \tag{26}$$

or

$$(.,.) = (.,.J)_n, \tag{27}$$

where $J = \det \boldsymbol{F}$ gives the change in volume. In addition, we also map the $\boldsymbol{\nabla}$ to $\boldsymbol{\nabla}_n$. The weak form now becomes: Find $\boldsymbol{u}, p$ and $\boldsymbol{x}$ such that

$$(((\boldsymbol{F}^{-T} \cdot \boldsymbol{\nabla}_n)\boldsymbol{v})^T, -\boldsymbol{\sigma} J)_n = -\Gamma\big((\boldsymbol{\nabla}\boldsymbol{v})^T, \boldsymbol{I} - \boldsymbol{n}\boldsymbol{n}\big)_S, \tag{28}$$

$$(q, (-\boldsymbol{F}^{-T} \cdot \boldsymbol{\nabla}_n) \cdot \boldsymbol{u} J)_n = 0, \tag{29}$$

$$((\boldsymbol{\nabla}_n \boldsymbol{w})^T, \boldsymbol{\nabla}_n \boldsymbol{x})_n = 0, \tag{30}$$

$$(\boldsymbol{r}, \frac{3\boldsymbol{x}^{n+1} - 4\boldsymbol{x}^n + \boldsymbol{x}^{n-1}}{2\Delta t} + (\boldsymbol{u} - \boldsymbol{u}_c) \cdot \boldsymbol{\nabla}_s \boldsymbol{x} - \boldsymbol{u}) = 0. \tag{31}$$

For the linearization we use that up to first order:

$$\delta \boldsymbol{F} = (\boldsymbol{\nabla}_n \delta \boldsymbol{x})^T, \tag{32}$$

$$\delta(\boldsymbol{F}^{-1}) = -\boldsymbol{F}^{-1} \cdot \delta \boldsymbol{F} \cdot \boldsymbol{F}^{-1} = -\boldsymbol{F}^{-1} \cdot (\boldsymbol{\nabla} \delta \boldsymbol{x})^T, \tag{33}$$

$$\delta J = J \boldsymbol{\nabla} \cdot \delta \boldsymbol{x}, \tag{34}$$

$$\delta \boldsymbol{g}^{\alpha} = -\boldsymbol{g}^{\alpha} \cdot \frac{\partial \delta \boldsymbol{x}}{\partial \xi_{\beta}} \boldsymbol{g}^{\beta}. \tag{35}$$

After linearization, that is we substitute $\boldsymbol{x}_i + \delta \boldsymbol{x}$, $p_i + \delta p$, $\boldsymbol{\tau}_i + \delta \boldsymbol{\tau}$, $\boldsymbol{F}_i^{-1} + \delta \boldsymbol{F}^{-1}$, $J_i + \delta J$, $\boldsymbol{g}_i^{\alpha} + \delta \boldsymbol{g}^{\alpha}$ and leave only first-order terms, we obtain the linearized weak form

$$\begin{aligned} &\big((\boldsymbol{\nabla}\boldsymbol{v})^T, -(\boldsymbol{\nabla}\delta\boldsymbol{x})^T \cdot \boldsymbol{\sigma} + \boldsymbol{\sigma}(\boldsymbol{\nabla} \cdot \delta\boldsymbol{x}) + \delta\boldsymbol{\tau}\big) - (\boldsymbol{\nabla} \cdot \boldsymbol{v}, p) + \Gamma(\boldsymbol{\nabla}_s \cdot \boldsymbol{v}, \boldsymbol{\nabla}_s \cdot \delta\boldsymbol{x})_S \\ &- \Gamma(\boldsymbol{\nabla}_s \boldsymbol{v}, \boldsymbol{\nabla}_s \delta\boldsymbol{x})_S = -\big((\boldsymbol{\nabla}\boldsymbol{v})^T, \boldsymbol{\tau}\big) - \Gamma\big(\frac{\partial \boldsymbol{v}}{\partial \xi^{\alpha}}, \boldsymbol{g}^{\alpha}\big)_S, \end{aligned} \tag{36}$$

$$\big(q, (\boldsymbol{\nabla}\delta\boldsymbol{x})(\boldsymbol{\nabla} \cdot \boldsymbol{u}) - \boldsymbol{\nabla} \cdot \delta\boldsymbol{u} - (\boldsymbol{\nabla} \cdot \boldsymbol{u})(\boldsymbol{\nabla} \cdot \delta\boldsymbol{x})\big) = (q, \boldsymbol{\nabla} \cdot \boldsymbol{u}), \tag{37}$$

where $p = p_i + \delta p$, $\boldsymbol{\sigma} = -p_i \boldsymbol{I} + \boldsymbol{\tau}_i$ and all subscripts $()_i$ have been dropped to increase readability. The surface tension term has been linearized and rewritten in terms of curvilinear coordinates, as follows

$$\Gamma\big((\boldsymbol{\nabla v})^T, \boldsymbol{I} - \boldsymbol{nn}\big)_S = \Gamma(\boldsymbol{\nabla}_s \cdot \boldsymbol{v}, \boldsymbol{\nabla}_s \cdot \delta\boldsymbol{x})_S - \Gamma(\boldsymbol{\nabla}_s \boldsymbol{v}, \boldsymbol{\nabla}_s \delta\boldsymbol{x})_S + \Gamma\big(\frac{\partial \boldsymbol{v}}{\partial \xi^\alpha}, \boldsymbol{g}^\alpha\big)_S. \quad (38)$$

Due to the presence of convection in the interface tracking it is essential to apply SUPG in order to stabilize it [17]. The terms that would arise from the variation of the stabilization term $\tau(\boldsymbol{u} - \boldsymbol{u}_c) \cdot \boldsymbol{\nabla}_s \boldsymbol{r}$, are generally omitted since they decrease the robustness of the Newton-Raphson method [18]. Thus, the linearized weak form of the interface tracking Eq. (31) becomes

$$\begin{aligned}
&(\boldsymbol{r}, \frac{3\delta\boldsymbol{x}}{2\Delta t}) + (\boldsymbol{r}, (\boldsymbol{u} - \boldsymbol{u}_\mathrm{c}) \cdot \boldsymbol{g}^\alpha \frac{\partial \delta\boldsymbol{x}}{\partial \xi^\alpha}) - (\boldsymbol{r}, (\boldsymbol{u} - \boldsymbol{u}_\mathrm{c}) \cdot \boldsymbol{g}^\alpha \cdot \frac{\partial \delta\boldsymbol{x}}{\partial \xi^\beta} \boldsymbol{g}^\beta \frac{\partial \boldsymbol{x}}{\partial \xi^\alpha}) \\
&+(\boldsymbol{r}, \delta\boldsymbol{u} \cdot \boldsymbol{g}^\alpha \frac{\partial \boldsymbol{x}}{\partial \xi^\alpha}) - (\boldsymbol{r}, \delta\boldsymbol{u}) + (\tau(\boldsymbol{u} - \boldsymbol{u}_\mathrm{c}) \cdot \boldsymbol{g}^\alpha \frac{\partial \boldsymbol{r}}{\partial \xi^\alpha}, \frac{3\delta\boldsymbol{x}}{2\Delta t}) \\
&-(\tau(\boldsymbol{u} - \boldsymbol{u}_\mathrm{c}) \cdot \boldsymbol{g}^\alpha \frac{\partial \boldsymbol{r}}{\partial \xi^\alpha}, \delta\boldsymbol{u}) \\
&+(\tau(\boldsymbol{u} - \boldsymbol{u}_\mathrm{c}) \cdot \boldsymbol{g}^\alpha \frac{\partial \boldsymbol{r}}{\partial \xi^\alpha}, (\boldsymbol{u} - \boldsymbol{u}_\mathrm{c}) \cdot \boldsymbol{g}^\gamma \frac{\partial \delta\boldsymbol{x}}{\partial \xi^\gamma}) \\
&-(\tau(\boldsymbol{u} - \boldsymbol{u}_\mathrm{c}) \cdot \boldsymbol{g}^\alpha \frac{\partial \boldsymbol{r}}{\partial \xi^\alpha}, (\boldsymbol{u} - \boldsymbol{u}_\mathrm{c}) \cdot \boldsymbol{g}^\gamma \cdot \frac{\partial \delta\boldsymbol{x}}{\partial \xi^\delta} \boldsymbol{g}^\delta \frac{\partial \boldsymbol{x}}{\partial \xi^\gamma}) \\
&+(\tau(\boldsymbol{u} - \boldsymbol{u}_\mathrm{c}) \cdot \boldsymbol{g}^\alpha \frac{\partial \boldsymbol{r}}{\partial \xi^\alpha}, \delta\boldsymbol{u} \cdot \boldsymbol{g}^\gamma \frac{\partial \boldsymbol{x}}{\partial \xi^\gamma}) \\
&= -(\boldsymbol{r}, \frac{3\boldsymbol{x} - 4\boldsymbol{x}^n + \boldsymbol{x}^{n-1}}{2\Delta t}) - (\boldsymbol{r}, (\boldsymbol{u} - \boldsymbol{u}_\mathrm{c}) \cdot \boldsymbol{g}^\alpha \frac{\partial \boldsymbol{x}}{\partial \xi^\alpha}) + (\boldsymbol{r}, \boldsymbol{u}) \\
&-(\tau(\boldsymbol{u} - \boldsymbol{u}_\mathrm{c}) \cdot \boldsymbol{g}^\alpha \frac{\partial \boldsymbol{r}}{\partial \xi^\alpha}, \frac{3\boldsymbol{x} - 4\boldsymbol{x}^n + \boldsymbol{x}^{n-1}}{2\Delta t}) \\
&+(\tau(\boldsymbol{u} - \boldsymbol{u}_\mathrm{c}) \cdot \boldsymbol{g}^\alpha \frac{\partial \boldsymbol{r}}{\partial \xi^\alpha}, \boldsymbol{u}) - (\tau(\boldsymbol{u} - \boldsymbol{u}_\mathrm{c}) \cdot \boldsymbol{g}^\alpha \frac{\partial \boldsymbol{r}}{\partial \xi^\alpha}, (\boldsymbol{u} - \boldsymbol{u}_\mathrm{c}) \cdot \boldsymbol{g}^\gamma \frac{\partial \boldsymbol{x}}{\partial \xi^\gamma}), \qquad (39)
\end{aligned}$$

where τ is the SUPG parameter given by

$$\tau = \frac{h}{2U}, \qquad (40)$$

with h the characteristic element length and $U = ||\boldsymbol{u}||$. Note, that $\boldsymbol{u}/U$ is a unit vector. To take into account the change of area, the right hand side of Eq. (39) is multiplied by $\boldsymbol{\nabla}_s \cdot \delta\boldsymbol{x}$ and subtracted from the left hand side. The complete system of equation can be written as follows

$$\begin{pmatrix} \underline{S} & \underline{L}^T & \underline{E} & \underline{E}_s + \underline{\Gamma}_S \\ \underline{L} & \underline{0} & \underline{G} & \underline{G}_S \\ \underline{0} & \underline{0} & \underline{P} & \underline{P}_S \\ \underline{X}_{u,S} & \underline{0} & \underline{0} & \underline{X}_{x,S} \end{pmatrix} \begin{pmatrix} \delta\underset{\sim}{u} \\ \underset{\sim}{p} \\ \delta\underset{\sim}{x} \\ \delta\underset{\sim}{x}_S \end{pmatrix} = \begin{pmatrix} \underset{\sim}{s} + \underset{\sim}{e} + \underset{\sim}{\gamma}_S \\ \underset{\sim}{l} + \underset{\sim}{g} \\ \underset{\sim}{h} \\ \underset{\sim}{x}_S \end{pmatrix}$$

The matrices $\underline{S}$ and $\underline{L}$ together with the corresponding right hand sides $\underline{s}$ and $\underline{l}$ represent the regular system for an incompressible Stokes flow. Matrices $\underline{E}, \underline{G}$ and vectors $\underline{e}, \underline{g}$ are the additional terms from the mapping of the integrals and gradients to a fixed volume. The contribution of the Poisson problem is given by $\underline{P}$ and $\underline{h}$. Finally, terms with the subscript $(.)_S$ involve only interface nodes where $\underline{X}_{x,S}, \underline{X}_{u,S}, \underline{x}_S$ are derived from the interface tracking Eq. (39) and $\underline{\Gamma}_S, \underline{\gamma}_S$ is the contribution of the surface tension Eq. (38) to the momentum balance.

4. Results

In this section, the convergence is demonstrated after which results are discussed for several different viscosity ratios as well as Ca numbers, where Ca is defined as $\mathrm{Ca} = \eta_c \dot{\gamma} R/\Gamma$. By using the inertia tensor $\mathcal{I}$ we can compute the principle axes of the deformed drop and compare directly with the Taylor deformation parameter D [1].

4.1. Calculation of deformation

Quantifying the deformation of the drop shape can be challenging, thus it is convenient to have a scalar measure of the deformation magnitude. As Taylor [1] suggested, this can be done by defining the dimensionless deformation parameter D as

$$D = \frac{a-b}{a+b}, \tag{41}$$

where a and b are the largest and smallest distances of the drop interface from its center respectively, as shown in Fig. 2. Thus, D is equal to zero for a sphere and becomes asymptotically unity for a slender drop. In order to quantify our results we first compute the second moment of inertia tensor $\mathcal{I}$ given by

$$\mathcal{I} = \int_\Omega \boldsymbol{x}'\boldsymbol{x}' d\Omega, \tag{42}$$

with $\boldsymbol{x}' = \boldsymbol{x} - \boldsymbol{x}_0$ where $\boldsymbol{x}_0$ is the center of mass of the drop. The inertia tensor can be rewritten using Gauss's theorem as an integral over a closed surface

$$\mathcal{I} = \int_\Omega \boldsymbol{x}'\boldsymbol{x}' d\Omega = \frac{1}{d+2}\int_\Omega \boldsymbol{\nabla}\cdot(\boldsymbol{x}'\boldsymbol{x}'\boldsymbol{x}') d\Omega = \frac{1}{d+2}\oint_S (\boldsymbol{n}\cdot\boldsymbol{x}')\boldsymbol{x}'\boldsymbol{x}' dS, \tag{43}$$

where d is the dimension of space. After diagonalization, the principle eigenvectors and eigenvalues of the inertia tensor provide a suitable measure for consistent calculation of the principle axes of the ellipsoid as well as the inclination angle θ. From the eigenvalues $\Lambda_1, \Lambda_2, \Lambda_3$ of $\mathcal{I}$, with $\Lambda_1 > \Lambda_2 > \Lambda_3$, one can compute $a = \sqrt{5\Lambda_1}, b = \sqrt{5\Lambda_3}$ and $c = \sqrt{5\Lambda_2}$ and thus calculate the Taylor deformation parameter D.

4.2. Convergence

To verify our numerical method we perform spatial and temporal convergence. For all the convergence tests we choose $\mathrm{Ca} = 0.3$ and $\lambda = 1$. Five different meshes are used with a varying number of elements on the drop equator, $n_\mathrm{e} = 10, 20, 30, 40$ and 120. To

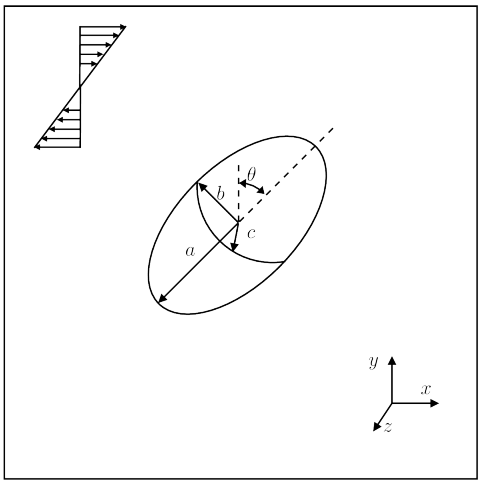

Fig. 2: Schematic representation of a single drop undergoing simple shear flow, with a, b and c the axes of the ellipsoid that the drop assumes and θ the inclination angle.

study the convergence of the method we calculate the relative errors for the deformation parameter e_{r}, which is given by

$$e_{\mathrm{r}} = \frac{|D^h - D^*|}{|D^*|},$$

where D^h is the solution on each of the meshes with different n_{e} and D^* is the reference solution using the finest mesh. In Fig. 3, a slope of three can be seen which is expected from the second-order elements that are used. We now fix the number of elements on the drop equator $n_{\mathrm{e}} = 30$ and vary the time step in order to study the temporal convergence. In Fig. 4, the relative error e_r of the solutions with time steps $\Delta t\dot{\gamma} = 10^{-3}, 5 \times 10^{-4}, 2.5 \times 10^{-4}, 10^{-4}$ relative to the solution obtained with a time step of $\Delta t\dot{\gamma} = 10^{-5}$. As expected, a slope of two can be seen, which is in agreement with the second-order time integration that is being used. In the remainder of this article, the number of elements on the drop equator will be fixed to $n_e = 30$ and the time step to $\Delta t\dot{\gamma} = 10^{-3}$ in order to maintain high accuracy, but without extreme computational cost.

One of the advantages of using the Newton-Raphson method to solve our non-linear system of equations is the fast convergence that it offers, which ideally should be quadratic. In Fig. 5, the convergence of the iterative scheme can be seen for the case of Ca $= 0.3$ and $\lambda = 1$. It is apparent that the convergence rate is linear and not quadratic, but with a large factor. One of the factors that can affect the convergence of the method is the fact that variation of the term $\tau(\boldsymbol{u} - \boldsymbol{u}_c) \cdot \boldsymbol{\nabla}_s \boldsymbol{r}$ in the discretized weak form of the interface tracking Eq. 39 has been neglected. After numerical experimentation we have found that the surface tension has a big effect on the convergence rate. When surface tension dominates the flow dynamics, smaller convergence rate is achieved. This dependence of the convergence rate of the iterative scheme on the capillary number can be seen in Fig. 6, for the case of $\lambda = 1$. It is apparent that as the capillary num-

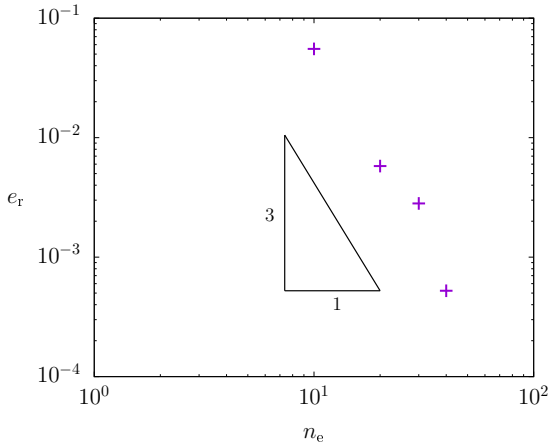

Fig. 3: Relative error e_r of D using different meshes with the number of elements on the equator of the drops being $n_\mathrm{e} = 10, 20, 30, 40$ marked with (+), at $t\dot{\gamma} = 0.01$. As a reference value we use the result obtained from the case of $n_\mathrm{e} = 120$. The triangle with side lengths of 3 and 1 is used to indicate the third order convergence.

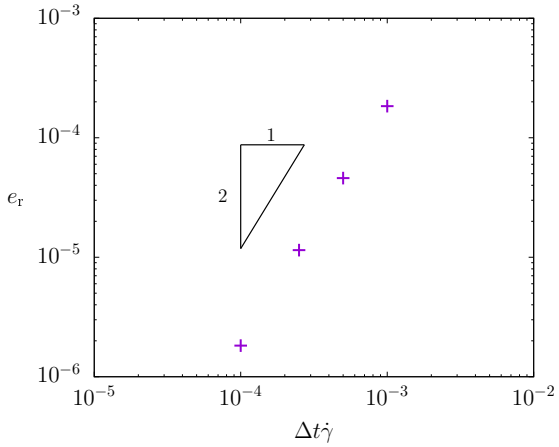

Fig. 4: Relative error e_r of D using different time steps at $t\dot{\gamma} = 0.01$. The error is plotted for the cases of $\Delta t\dot{\gamma} = 10^{-3}, 5\times10^{-4}, 2.5\times10^{-4}, 10^{-4}$, marked with (+), relative to the one obtained with $\Delta t\dot{\gamma} = 10^{-5}$. The triangle with side lengths of 2 and 1 is used to indicate the second order convergence.

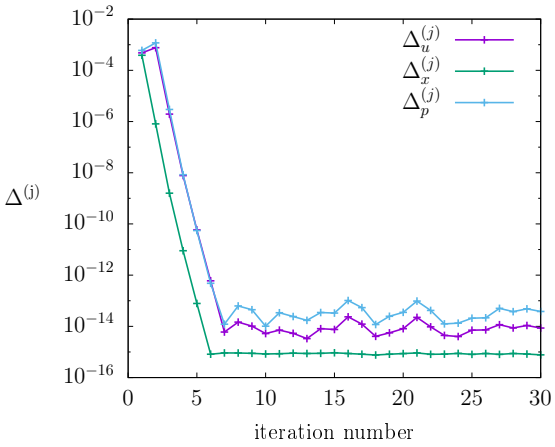

Fig. 5: Difference between the Newton-Raphson iterations for the case of Ca = 0.3 and $\lambda = 1$.

ber decreases, i.e. the surface tension forces become dominant, the convergence rate of the positions decreases substantially. One of the drawbacks of Newton-Raphson is the small convergence region that could lead into divergence of the scheme. In that case, a Picard scheme can be used, for example by computing the Jacobian only during the first iteration and keeping it constant until the method has converged.

4.3. Transient deformation

Due to the applied shear flow, the drop starts to deform until it reaches a steady ellipsoidal shape with a fixed orientation with regard to the flow direction. Typical results obtained from our simulations that show the transient response of the drop interface can be seen in Fig. 7. For the case of Ca = 0.3 and $\lambda = 5$ an initial spherical drop, shown in Fig. 7a, starts to deform under the applied shear rate. Figs. 7b-c show the position of the interface at time $\Delta t\dot{\gamma} = 0.2$ and 0.8 respectively until the final shape is obtained as shown in Fig. 7d.

The non-dimensionless axes $a/2R, b/2R$ and $c/2R$ that are calculated from the second moment of inertia tensor for the case of Ca = 0.1 and $\lambda = 1$ can be seen in Fig. 8. Initially, they are equal to the diameter $2R$ of the spherical drop until shear rate is applied and the drop starts to deform. The axis a shows the increase of the largest distance of the drop interface from its center, whereas the axis b gives the smallest distance which decreases over time. It is evident that the ratio of the axes out of the flow plane c over b, as show in Fig. 9, differs from the value of 1, meaning that the drop cross section may deviate from the axisymmetric case. Consequently, from the initial value of zero, D starts to increase over time reaching a stationary value of 0.11 as shown in Fig. 10. The evolution of the inclination angle θ for the same case can be seen in Fig. 11. Noticeably, θ is not defined for a perfectly spherical drop at rest, but right after it gets deformed, θ starts from values of approximately 45° and then gradually increases until the steady state is reached with a value of 51.46°. The time needed for the drop to reach the steady-state shape increases with increasing Ca number.

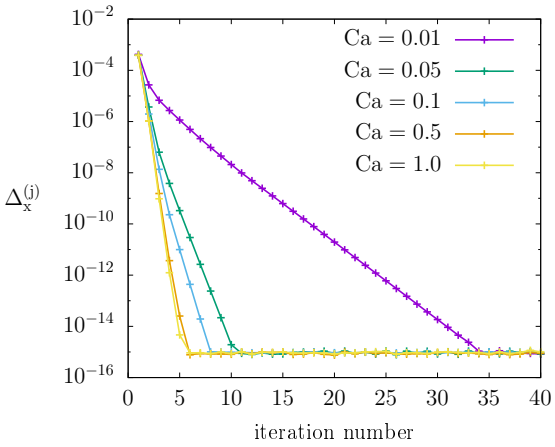

Fig. 6: Dependence of the convergence rate of positions on the capillary number for the case of $\lambda = 1$.

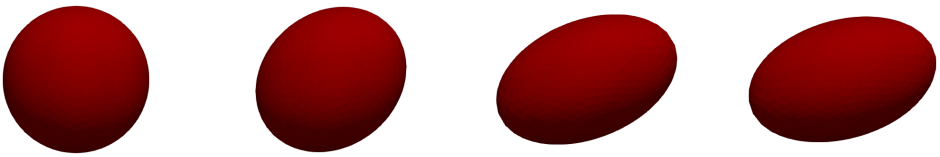

(a) (b) (c) (d)

Fig. 7: Transient drop motion with Ca = 0.3 and $\lambda = 5$ at different times. a) Initially undeformed drop at $t\dot{\gamma} = 0$, b) transient drop shape at $t\dot{\gamma} = 0.2$ and c) at $t\dot{\gamma} = 0.8$, d) final shape at $t\dot{\gamma} = 2$.

4.4. Steady-state deformation

In Fig. 12, the shape of the droplet at the steady state for a range of Ca and λ can be seen. For the limiting case of Ca = 0 the shape of the drop would remain perfectly spherical representing a solid sphere. The effect of the Ca on the drop shape can be seen in Figs. 13 and 14, where we plot D and θ as a function of Ca for $\lambda = 5.0$. When Ca increases, the drop starts to deform and turns into an ellipsoid while the inclination angle θ starts to increase from the 45°. Comparing the results with the theory for small deformations of Taylor [1], we can see in Fig. 15 for Ca = 0.01 and $\lambda = 1$ that there is a good agreement. In Fig. 16 the inclination angle θ for the same case can be seen, which already starts to differ from Taylor's theory assumption of $\theta = 45°$. Looking at the effect of the viscosity ratio λ on the deformation parameter D for the case of Ca = 0.2, it can be seen, in Fig. 17, that D is initially increasing until it reaches a maximum value around $\lambda = 1$ and then decreases again. On the other hand, the inclination angle θ continuously increases for the range of λ values that we studied, as shown in Fig. 18.

The effects of the presence of walls are not under consideration in this work. These

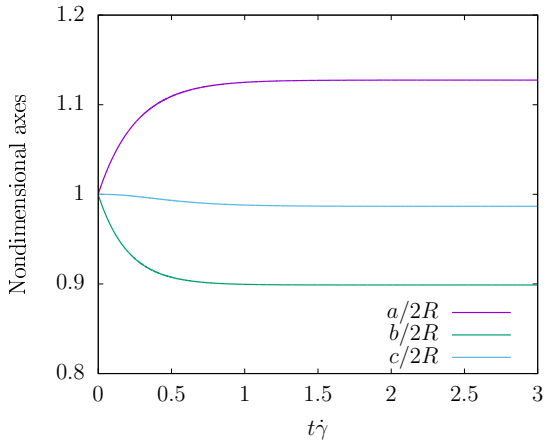

Fig. 8: Evolution of the three axes of the ellipsoid with respect to the initial diameter of the drop for the case of Ca = 0.1 and $\lambda = 1$.

effects have been studied extensively in the literature, as an example we refer to [19, 5]. It is possible to minimize such effects by imposing tri-periodic boundary conditions similar to Jaensson *et al.* [20], but in order to evaluate our method we choose to simplify our study case by including the walls.

5. Conclusions

We have presented 3D simulations of a viscous drop suspended in a viscous matrix under shear flow. A sharp interface was used for the interface tracking problem where the nodes move only in the normal direction. This way we were able to simulate our problem without the need of frequently remeshing. Furthermore, the update of the interface and the bulk mesh nodes is coupled with the flow problem allowing us to overcome time step limitations that the mesh capillary time imposes. The non-linear system of equations was linearized and solved with the Newton-Raphson method. Although the convergence of the iterative method was fast, we could not find a region of quadratic convergence. After numerical experimentation, we found that the surface tension plays a major role on the convergence, but in order to better understand these effects, further research is required.

The problem of the isolated drop deforming under simple shear has been extensively studied in the literature [2, 3] and is a good case to validate our model. Using the second moment of the inertia tensor we were able to calculate the principle axes of the ellipsoidal shape of the drop. This way it was possible to calculate the dimensionless deformation parameter D and inclination angle θ of Taylor [1]. Comparing our results for small Ca with the theory for small deformations [1], we could see that there was a good agreement.

It is worth noting that implicit implementations that require costly solutions of non-linear system of equations like the one presented here, are not always more efficient than their explicit counterparts. An implicit method where the interface tracking is coupled with the flow problem is a powerful tool which can give great physical inside in certain

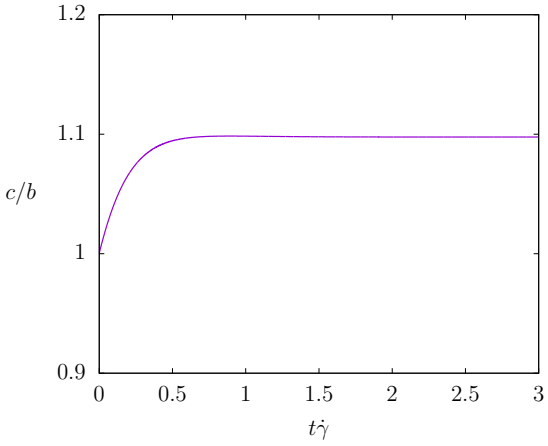

Fig. 9: Aspect ratio c/b as a function of time for the case of Ca $= 0.1$ and $\lambda = 1$.

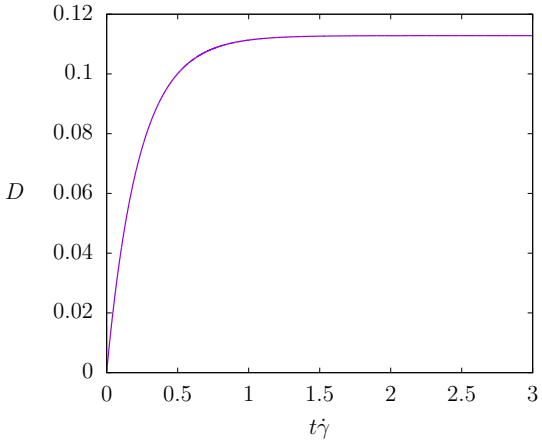

Fig. 10: Deformation parameter D as a function of time for the case of Ca $= 0.1$ and $\lambda = 1$.

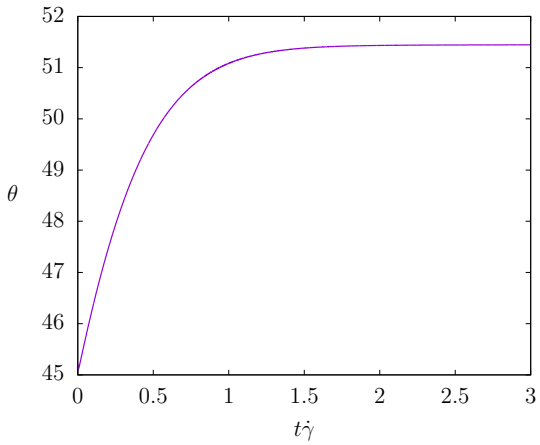

Fig. 11: Inclination angle θ as a function of time for the case of Ca $= 0.1$ and $\lambda = 1$.

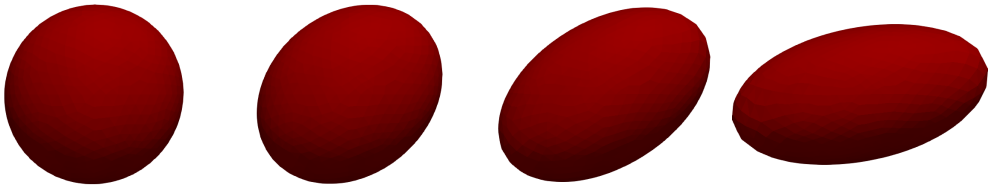

Fig. 12: Steady state drop profiles for different Ca and λ values. a) Ca $= 0.01, \lambda = 0.01$, a) Ca $= 0.1, \lambda = 0.5$, a) Ca $= 0.2, \lambda = 1.0$, a) Ca $= 0.5, \lambda = 5.0$.

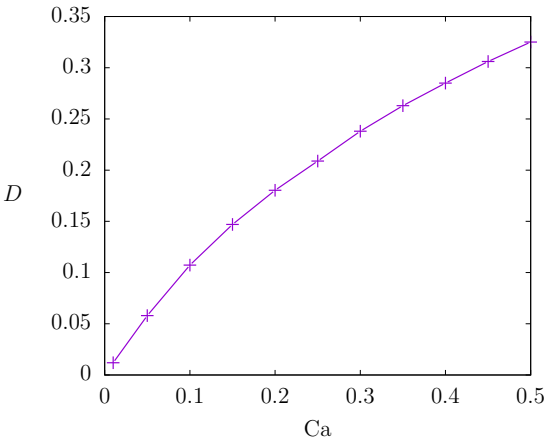

Fig. 13: Deformation parameter D as a function of Ca number with a constant viscosity ratio of $\lambda = 5.0$.

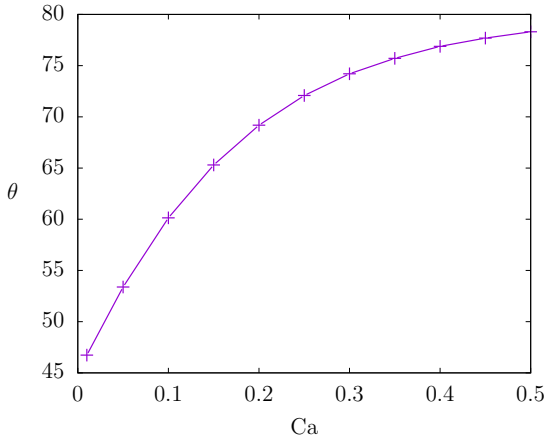

Fig. 14: Inclination angle θ as a function of Ca number with a constant viscosity ratio of $\lambda = 5.0$.

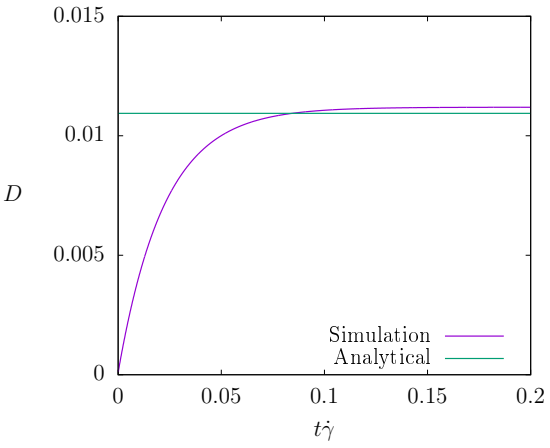

Fig. 15: Deformation parameter as a function of time for the case of Ca = 0.01 and $\lambda = 1$. The straight line indicates the steady state value predicted by the small deformation theory of Taylor [1].

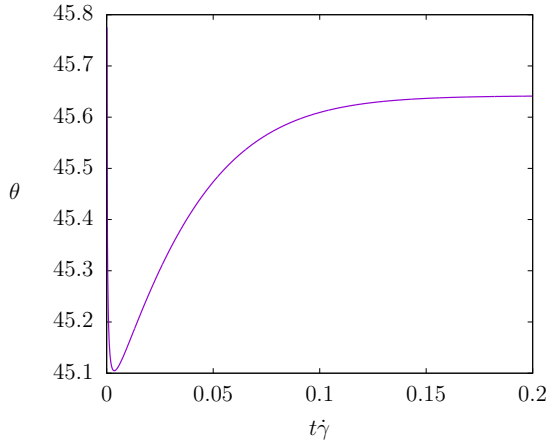

Fig. 16: Inclination angle as a function of time for the case of Ca = 0.01 and $\lambda = 1$.

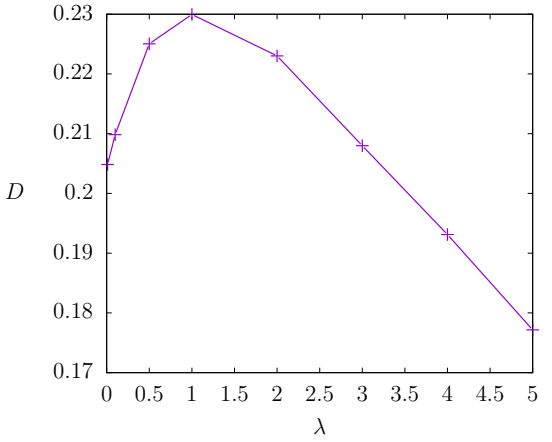

Fig. 17: Deformation parameter as a function of viscosity ratio with a constant Ca = 0.2.

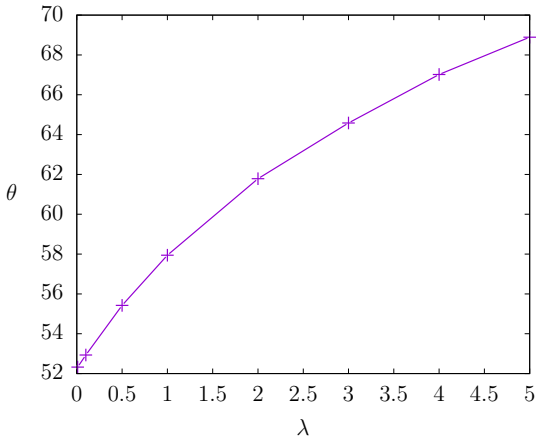

Fig. 18: Inclination angle as a function of viscosity ratio with a constant Ca = 0.2.

classes of problems. For example, in cases where material interfaces are close to each other and fine meshes are required, using an implicit method can help overcome time step limitations. However, when the surface tension is dominant, the convergence rate of the iterative scheme can be reduced.

Acknowledgment

The research leading to these results has received funding from the European Commission under the grant agreement number 604271 (Project acronym: MoDeNa; call identifier: FP7-NMP-2013-SMALL-7).

References

[1] G. I. Taylor, "The Formation of Emulsions in Definable Fields of Flow," *Proceedings of the Royal Society A: Mathematical, Physical and Engineering Sciences*, vol. 146, pp. 501–523, oct 1934.

[2] J. M. Rallison, "The Deformation of Small Viscous Drops and Bubbles in Shear Flows," *Annual Review of Fluid Mechanics*, vol. 16, no. 1, pp. 45–66, 1984.

[3] H. A. Stone, "Dynamics of Drop Deformation and Breakup in Viscous Fluids," *Annual Review of Fluid Mechanics*, vol. 26, no. 1, pp. 65–102, 1994.

[4] L. A. Utracki, *Polymer Alloys and Blends: Thermodynamics and Rheology*. Hanser Gardner Publications, 1990.

[5] M. Kennedy, C. Pozrikidis, and R. Skalak, "Motion and deformation of liquid drops, and the rheology of dilute emulsions in simple shear flow," *Computers & Fluids*, vol. 23, pp. 251–278, feb 1994.

[6] N. O. Jaensson, M. A. Hulsen, and P. D. Anderson, "On the use of a diffuse-interface model for the simulation of rigid particles in two-phase Newtonian and viscoelastic fluids," *Computers and Fluids*, vol. 156, pp. 81–96, 2017.

[7] T. E. Tezduyar, "Interface-tracking and interface-capturing techniques for finite element computation of moving boundaries and interfaces," *Computer Methods in Applied Mechanics and Engineering*, vol. 195, no. 23-24, pp. 2983–3000, 2006.

[8] M. M. Villone, M. A. Hulsen, P. D. Anderson, and P. L. Maffettone, "Simulations of deformable systems in fluids under shear flow using an arbitrary Lagrangian Eulerian technique," *Computers and Fluids*, vol. 90, pp. 88–100, 2014.

[9] R. Courant, K. Friedrichs, and H. Lewy, "On the Partial Difference Equations of Physics," *IBM Journal of Research and Development*, vol. 11, no. 2, pp. 215 – 234, 1967.
[10] J. M. Rallison and A. Acrivos, "A numerical study of the deformation and burst of a viscous drop in an extensional flow," *Journal of Fluid Mechanics*, vol. 89, p. 191, nov 1978.
[11] Y. Wang and P. Dimitrakopoulos, "A three-dimensional spectral boundary element algorithm for interfacial dynamics in Stokes flow," *Physics of Fluids*, vol. 18, no. 8, 2006.
[12] A. Villa and L. Formaggia, "Implicit tracking for multi-fluid simulations," *Journal of Computational Physics*, vol. 229, no. 16, pp. 5788–5802, 2010.
[13] S. Basting and M. Weismann, "A hybrid level set/front tracking approach for finite element simulations of two-phase flows," *Journal of Computational and Applied Mathematics*, vol. 270, pp. 471–483, 2014.
[14] R. Nourgaliev, S. Kadioglu, and V. Mousseau, "Fully-Implicit Interface Tracking for All-Speed Multifluid Flows," in *Computational Fluid Dynamics 2008*, pp. 551–557, Berlin, Heidelberg: Springer Berlin Heidelberg, 2009.
[15] H. L. Goldsmith and J. Marlow, "Flow Behaviour of Erythrocytes. I. Rotation and Deformation in Dilute Suspensions," *Proceedings of the Royal Society B: Biological Sciences*, vol. 182, no. 1068, pp. 351–384, 1972.
[16] N. O. Jaensson, M. A. Hulsen, and P. D. Anderson, "Stokes-Cahn-Hilliard formulations and simulations of two-phase flows with suspended rigid particles," *Computers and Fluids*, vol. 111, pp. 1–17, 2015.
[17] A. N. Brooks and T. J. Hughes, "Streamline upwind/Petrov-Galerkin formulations for convection dominated flows with particular emphasis on the incompressible Navier-Stokes equations," *Computer Methods in Applied Mechanics and Engineering*, vol. 32, no. 1-3, pp. 199–259, 1982.
[18] P. Knechtges, "The fully-implicit log-conformation formulation and its application to three-dimensional flows," *Journal of Non-Newtonian Fluid Mechanics*, vol. 223, pp. 209–220, sep 2015.
[19] W. S. J. Uijttewaal and E. J. Nijhof, "The motion of a droplet subjected to linear shear flow including the presence of a plane wall," *Journal of Fluid Mechanics*, vol. 302, p. 45, nov 1995.
[20] N. O. Jaensson, M. A. Hulsen, and P. D. Anderson, "Simulations of the start-up of shear flow of 2D particle suspensions in viscoelastic fluids: Structure formation and rheology," *Journal of Non-Newtonian Fluid Mechanics*, vol. 225, pp. 70–85, 2015.